



# Use of portable X-ray fluorescence instrument for bulk alloy analysis on low corroded indoor bronzes



D. Šatović<sup>a,\*</sup>, V. Desnica<sup>a</sup>, S. Fazinić<sup>b</sup>

<sup>a</sup> Department of Conservation and Restoration, Academy of Fine Arts, Ilica 85, 10000 Zagreb, Croatia

<sup>b</sup> Laboratory for Ion Beam Interactions, Ruđer Bošković Institute, Bijenička 54, 10000 Zagreb, Croatia

## ARTICLE INFO

### Article history:

Received 3 May 2013

Accepted 20 August 2013

Available online 30 August 2013

### Keywords:

X-ray fluorescence analysis

Non-destructive analysis

Corrosion

Bronze

Archaeometry

## ABSTRACT

One of the most often used non-destructive methods for elemental analysis when performing field measurements on bronze sculptures is X-ray fluorescence (XRF) analysis based on portable instrumentation. However, when performing routine in-situ XRF analysis on corroded objects obtained results are sometimes considerably influenced by the corrosion surface products.

In this work the suitability of portable XRF for bulk analysis of low corroded bronzes, which were initially precisely characterized using sophisticated and reliable laboratory methods, was investigated and some improvements in measuring technique and data processing were given. Artificially corroded bronze samples were analyzed by a portable XRF instrument using the same methodology and procedures as when performing in-situ analysis on real objects. The samples were first investigated using sophisticated complementary laboratory techniques: Scanning Electron Microscopy, Proton-Induced X-ray Emission Spectroscopy and Rutherford Backscattering Spectrometry, in order to gain precise information on the formation of the corrosion product layers and in-depth elemental profile of corrosion layers for different aging parameters. It has been shown that for corrosion layers of up to ca. 25  $\mu\text{m}$  a portable XRF can yield very accurate quantification results.

© 2013 Elsevier B.V. All rights reserved.

## 1. Introduction

Bronze artifacts are vulnerable to outdoor and indoor corrosion environments – from acid rain containing sulfates and carbonates in urban–industrial environment, to chlorides in marine environmental exposure, which are main cause of “bronze disease” [1,2]. Indoor corrosion environments (museums) are less aggressive, however, it has been reported that indoor corrosion seems to be affected by a greater number of air pollutants than the outdoor corrosion, especially when indoor sources of corrodents are present [3].

Chloride ions and sulfur compounds are the most common and important atmospheric corrosive agent, as has been reported [4]. Chloride ions can contribute to many corrosion problems associated with museum objects and can originate from different sources: from soil (archaeological bronzes), human perspiration or from materials and objects that contains chlorinated compounds.

In addition, bronze artifacts are usually very heterogeneous in composition, and thus various corrode forming and inhomogeneous corrosion product surface layers (patinas) [5]. To get full information of ongoing corrosion processes on the bronze surface it is essential to know composition (and structure) of the original bronze material (intrinsic corrosion parameters) [6].

Handling archaeological, historical or recent artistic bronzes demands some special conservation–restoration requirements when it comes to choosing a measurement method: (i) the method should be non-destructive (only small sample can be taken and it should not be destroyed during measurements) or (ii), preferably, the method should be non-invasive (measurements should be done on the object without sampling). This is especially important when it comes to small plastic bronze objects with fine ornamental or figural relieve.

Nevertheless, surface treatments prior to measurement (especially for techniques such as Proton-Induced X-ray Emission Spectroscopy (PIXE) or X-ray fluorescence Spectrometry, XRF) still include the washing of bronze in formic acid followed by glass bristle brushing [7] or abrading using a corundum burr [8] or a rotating rubber tip, impregnated with alumina grains as abrasive [9] for the micro-polishing.

Furthermore, it has been demonstrated by Swann et al. [8] that the mentioned surface treatment of copper archaeological objects does not insure that the area of analysis is corrosion free. They have noted that even bright-colored metal may not be sufficiently corrosion free to satisfy the needs of the techniques such as PIXE and XRF. From the standpoint of the restoration–conservation practice, any aggressive cleaning of these objects has been determined to be an unacceptable intrusion to the object. It is, therefore, a great advantage to be able to analyze bulk metal composition of bronze artifacts without disrupting patina formed on surface. When investigating bronze corrosion products, where the patina layers can reach thicknesses of 1–2 mm, and the X-ray penetration depth is limited to max. 100–200  $\mu\text{m}$ , XRF can

\* Corresponding author. Tel./fax: +385 14821138.

E-mail address: [dsatovic@alu.hr](mailto:dsatovic@alu.hr) (D. Šatović).

essentially be regarded to as a surface technique. Therefore, there is a reasonable concern that measurements can be affected by the presence of corrosion product layers which could not be removed due to conservation–restoration requirements. As it is known, the influence of corrosion processes on data reliability in some cases (archaeological bronzes with thick corrosion layers) can be significant [8]. However, if the thickness of the corrosion layer is very small, analytical techniques revealing the chemical composition of the bulk, like X-ray fluorescence, may be applied [10–13].

Of course, one should be aware that there may be other factors affecting the suitability of surface techniques such as XRF for bulk analysis, e.g. electrochemical deterioration of bronze surface exposed to the seawater [14], or particle size and surface irregularity effects [15], but here we investigate only the effects due to corrosion. Only one technique, Prompt Gamma Activation Analysis, can provide the composition of the bulk of corroded metal [16], but the necessary decay time after activation involves additional problems.

The purpose of this work is to explore the contributions that quantitative elemental analysis using portable XRF can make (to resolve these questions) within the constraints that the analysis has to be totally non-invasive. We concentrate on the corrosive environmental processes which lead to the formation of a smooth, usually brown–reddish thin corrosion layers characterized as type I. corrosion processes [17]. These types of corrosion layers form usually in low aggressive conditions such as museum environment or other indoor environments.

The samples were first investigated using sophisticated and reliable laboratory methods: Scanning Electron Microscopy (SEM), micro-PIXE and Rutherford Backscattering Spectrometry (RBS) in order to gain precise information on the formation of the corrosion product layers and in-depth elemental profile of the corrosion layer. Precise characterization of the corrosion layers was essential for exact interpretation of XRF spectra which allowed assessment of capability of portable XRF equipment for the quantitative bulk analysis of corroded bronze objects. The possibilities and limitations of micro-XRF portable spectrometer in the analysis of low corroded bronze artifacts are also discussed.

## 2. Materials and methods

CuSn6 binary bronze alloy was chosen as it is commonly used for artistic castings. The bronze CuSn6 coupons, sized  $5.0 \times 3.0 \times 0.3$  cm, were cut out from the standard certificated alloy (Cu 93.66 wt.%; Sn 6.10 wt.%; P 0.11 wt.%; Zn 0.10 wt.%; Fe 0.02 wt.%; and Pb 0.01 wt.%). Corrosion layers were formed artificially by immersion in 0.012 M sodium–chloride solution (0.7 g/l NaCl aqueous solution) simulating chloride corrosion environment for a specified period of time (longest immersion time was 60 days). In this way we were able to get well formed and defined corrosion layers. Solution of 0.012 M NaCl was chosen to simulate the type of pollutants found in museum environments [18]. Coupons were taken out every 24 h successively for a period of 1 to 60 days, dried and stored in desiccator. Prior to immersion, the coupons were mechanically treated with P 800 abrasive paper, then polished with P 1200 paper, degreased with ethanol, immersed in 10% (wt) H<sub>2</sub>SO<sub>4</sub> for 3 min and finally dried at room temperature. All corrosion layer formation experiments were carried out in a 1 dm<sup>3</sup> laboratory vessel, at room temperature ( $25 \pm 1$  °C). The volume-to-surface specimen area was 20 mL cm<sup>-2</sup> according to the ASTM G 31 (1990) standard [19].

The Philips XL 30 scanning electron microscope (SEM) was used to present secondary electron images of the samples surfaces – related images show surface morphology and we have not performed Energy Dispersive X-ray Spectroscopy analysis since the penetration depths of the incoming electrons are such that the related X-ray depth information is just at the level of about one micrometer.

PIXE and RBS measurements were performed using 2 MeV proton beam from the 1.0 MV Tandetron electrostatic accelerator at the

Ruder Bošković Institute (RBI) in Zagreb. The measurements were performed at the general purpose ion beam analysis chamber, and at the ion microbeam. At the general purpose ion beam analysis end-station PIXE spectra were recorded by two solid state silicon detectors. The detector dedicated for recording higher energy parts of PIXE spectra is 80 mm<sup>2</sup> Canberra Si (Li) detector with rather large working solid angle (0.03 sr). At the same time, low energy parts of PIXE spectra were detected by 10 mm<sup>2</sup> Ketek SDD detector having 8 μm Be window and small solid angle (0.0005 sr), with the installed permanent magnet system for deflection of backscattering protons to prevent their detection by the SDD detector. Si (Li) detector is positioned at 135° scattering angle in horizontal plane, while SDD detector is positioned at 150° scattering angle in vertical plane. An RBS detector (0.01 sr) installed in vertical plane at the scattering angle of 165° was used to record proton backscattered spectra. The accelerated proton beam coming from the accelerator into the end-station was collimated by the set of circular collimators to the diameter of 3 mm. Data from detectors were collected by using conventional charged particle spectroscopy chain connected to the homemade multiparameter data acquisition and analysis system SPECTOR [20]. Measured elastic backscattering spectra were analyzed by using reliable and well known ion beam analysis and simulation software SIMNRA [21]. For the analysis we used evaluated elastic backscattering cross sections for 12C(p,p)12C and 16O(p,p)16O calculated using the on-line SIGMACALC calculator [22] for the scattering angle of 165°. Measured PIXE spectra were analyzed using PIXE analysis software GUPIXWIN, the Windows version of the well known and reliable GUPIX software [23].

At the RBI ion microbeam facility [24], 2 MeV proton beam of about 50 pA current was focused to μm dimensions. The beam was scanned over the samples by the computer-controlled scan generator. The copper mesh with repetition of 25 μm was used to check the beam diameter and to adjust the scanned area to  $50 \times 50$  μm<sup>2</sup>. Areal and lateral scans over the samples were performed to investigate the corrosion layers. For this purpose a small specimen cut from samples after 0, 14 and 26 days of immersion was embedded in epoxy resin and polished with paper grade P1200 in order to obtain clearly visible cross sections. The proton beam used for scanning was focused to 2.5 μm. The collection time for each two-dimensional (2D) elemental map was about 20 min. 2D elemental maps for copper and tin were created using the homemade SPECTOR data acquisition and analysis software. Penetration depth of 2 MeV protons in Cu is about 18.3 μm and 27.5 μm in CuO (calculated by SRIM code). Proton microbeam X-ray elemental images presented were taken on the sample cross sections. During the scanning the proton beam was passing through the pure Cu matrix or at the surface through the corrosion layer matrix (mainly Cu oxides). RBS measurements were taken with the surface of the samples being perpendicular to the beam (i.e. the beam was first passing through the Cu oxide layers and fully stopped in Cu bulk).

The samples were then investigated using a portable XRF instrument, which was developed at the Laboratory of the Academy of fine arts in Zagreb. It consists of a 50-kV Rh excitation tube, a Peltier-cooled silicon drift detector with energy resolution of 145 eV at the Mn K $\alpha$  excitation line. Depending on the analytical needs, the device can provide either mili or micro X-ray beam for sample excitation, by employing a motorized collimator interchanger to switch between a pinhole collimator (spot size ca. 1.5 mm) and a polycapillary lens (spot size ca. 45 μm). The operating parameters for tube voltage and anode current during the measurements were set to 40 keV and 150 μA, respectively, and the acquisition real time was 200 s. The diameter of the beam was set to 1.5 mm. Quantitative analysis of the XRF spectra was performed using the XRF-FP software from Amptek, USA, based on the fundamental parameter approach. To minimize errors in quantitative analysis due to improper matrix X-ray absorption correction a calibration of individual elemental sensitivities was performed. The calibration coefficients were obtained from a measurement of a known CuSn6 reference material.

### 3. Results and discussion

#### 3.1. Formation of the corrosion layers on bronze and spectroscopic examination of the surface morphology

SEM investigation was employed to determine corrosion layers formation through the observation of surface morphology. Based on SEM micrographs the specimens of 14 and 26 days of immersion were chosen as a representative specimens for further measurement since no significant change in surface morphology could be noticed after 26 days of immersion. Fig. 1 shows formed corrosion layers after 0, 14 and 26 days of exposure. Already after several hours of exposure to sodium chloride solution, the transparent greenish layer with metallic luster is clearly visible on the bronze surface. After 14 days of exposure this layer becomes more opaque but still has metallic luster (Fig. 1b). As immersion time increases, a new, brownish–purple layer is forming on the surface (Fig. 1b, lower right corner of the coupon). This layer seems to be formed above the existing green layer and becomes more opaque and darker with further exposure and reaches full saturation after 26 days of immersion (Fig. 1c). As can be seen, formation of corrosion products on the surface of the coupons is quite inhomogeneous and uneven. After 26 days of exposure, both dark purple and green corrosion products are present on the coupon surface (Fig. 1c).

SEM micrographs reveal morphology and structure of the successive corrosion layers formation (Fig. 2). Crystalline shell-like structures evenly distributed over the surface are clearly visible after 14 days of exposure (Fig. 2b). These structures correspond to greenish translucent layer visible on the surface of the coupon. However, on the Fig. 2c, only regular spherical shapes are clearly visible, which, with the increasing time of exposure, become more densely distributed but generally the same size and shape during the whole exposure time. As it can be seen on Fig. 2c, the contours of primary formed shell-like structures can be noticed under these spherical structures. It seems that these secondary structures grow upon primary formed shell-like structures. According to literature [25], such forms are a mixture of copper oxide compounds. SEM results clearly indicate the formation of the two-layered corrosion structure on the bronze surface with the significant retardation of the further corrosion rate after formation of a second layer. Corrosion layers of 14th and 26th day coupons were taken as a representative corrosion layers that usually forms in low aggressive environment.

#### 3.2. Cross-section elemental distribution of the corrosion layers and in-depth composition by PIXE and RBS

Micro-PIXE analysis was performed in order to obtain elemental distribution of the cross-sections of the corrosion product layers formed on bronze. For that purpose a small specimen cut from a non-corroded coupon as well as from 14th and 26th day coupon was embedded in epoxy resin and polished to gain clear cross-section. Fig. 3a) shows PIXE copper and tin elemental distributions in the cross-sections of the bronze samples. The gray zones at the lower part of the elemental maps correspond to the epoxy resin in which the specimens were embedded. The two main zones can be clearly distinguished on all copper elemental maps: the bulk metal (yellow) and the corrosion product layer (bluish). The figure shows thin surface layer, light blue to dark blue areas which are evidently increasing in thickness during immersion time. At the same time, tin elemental maps (from Sn-L $\alpha$  intensity) show equal distribution of tin across the layer. Slightly uneven distribution of tin atoms can be observed only at the 26th day sample. Using the color scale attached to the elemental maps, tin concentration two times lower than in bulk can be estimated (Fig. 3a). Tin concentration is probably even lower than estimated if the lower attenuation of the Sn-L $\alpha$  radiation in lighter matrix (corrosion layer) is taken into account.

The micro-PIXE maps show clearly surface roughness and relatively large variations in corrosion layer thickness at this microscopic scale, for both 14th and 26th day samples. A total corrosion layer thickness of up to approx. 25  $\mu\text{m}$  could be estimated for 26th day sample. It seems from the 26th day map that corrosion layers are also at some points separated from each other.

The evidence of the surface roughness is also seen at the RBS spectra shown at the Fig. 3b, which shows RBS spectra (red dotted line) and fitted results with SIMNRA software (black solid line) for non-corroded bronze as well as for 14 and 26 day corroded bronze coupons. These RBS spectra were obtained by irradiation of the surface areas corresponding to a disc of 3 mm diameter. The spectra related to 14th and 26th day samples clearly show the sharp “knee” that stands out in the part of the fits (far right in the spectrum, at 1700 keV) which is a macroscopic evidence of the surface roughness and unevenness of the corrosion products on the surface as evidenced on SEM micrographs and micro-PIXE maps on the microscopic level. In principle the RBS technique can give information on the composition profile, i.e. distribution of the

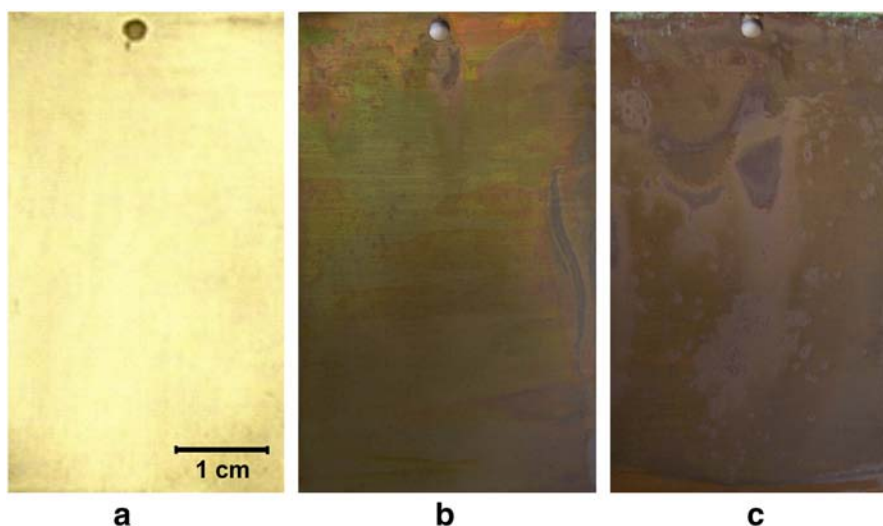


Fig. 1. Formation of corrosion layers on CuSn6 bronze coupons during the immersion in aqueous chloride solution (0.7 g/L NaCl); a) non-corroded coupon; b) 14 days of immersion, and c) 26 days of immersion. Dimensions of coupons: 5 × 3 × 0.3 cm.

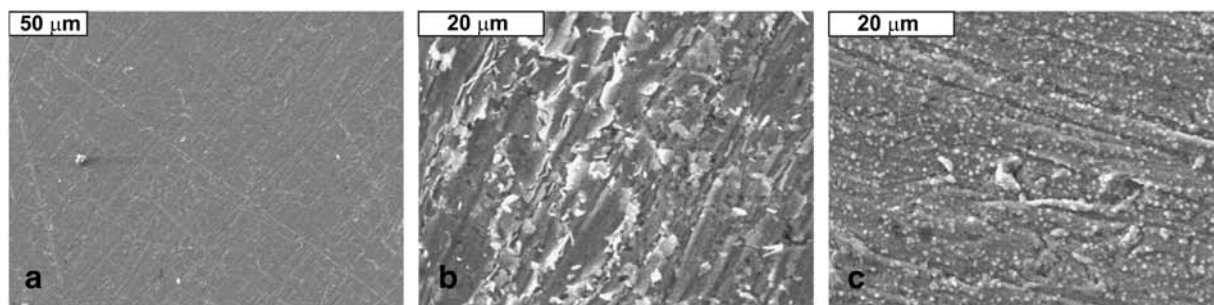


Fig. 2. SEM micrographs of the bronze surface after 0 (a), 14 (b), 26 (c) days of exposure to the aqueous chloride solution (0.7 g/l NaCl).

elements in the corrosion layer, allowing the relative composition of corrosion products in the layers to be found as well as thickness of each hypothetical layer. We used SIMNRA to fit the spectra in order to estimate corrosion layer profiles. However, due to the evidenced high surface roughness and unevenness of the corrosion products on the surface at microscopic scale (transferred to the macro scale as evidenced on the RBS spectra), the results obtained are only indicative and qualitative since the relative uncertainties in obtained layer thicknesses could be even more than 50%. Regarding the layer compositions, in fitting the spectra whenever possible we assumed stoichiometric compositions of copper and oxygen ( $\text{CuO}$ ,  $\text{Cu}_2\text{O}$ ) in layers.

Having all these assumptions and restrictions in mind, at Fig. 3b there is an evidence of a thin oxide corrosion layer on the 14 day

corroded bronze which was modeled using the composition of pure  $\text{CuO}$ . The best fit for 26 day corroded bronze was obtained assuming a three layer structure on the bulk of the bronze which is in good agreement with PIXE elemental map for the same sample. According to the fit, tin is present only in the first layer (closest to bulk), but in lower concentration than in bulk (2.7 wt.%). Other constituents of the layer are only copper and oxide, approximately in the 1:1 ratio. It can be concluded that the first layer is mostly composed of copper (II) oxide and tin (II) oxide. These oxides (copper and tin) are in the relatively same ratio as the bulk composition of the bronze. The second layer contains hydrogen together with copper and oxide atoms in 2.5:1.5:1.0 (Cu:O:H) ratio. It can be reasonably assumed, that this secondary layer is probably composed of hydrated copper (I) and copper (II) oxides i.e. cuprite ( $\text{Cu}_2\text{O}$ )

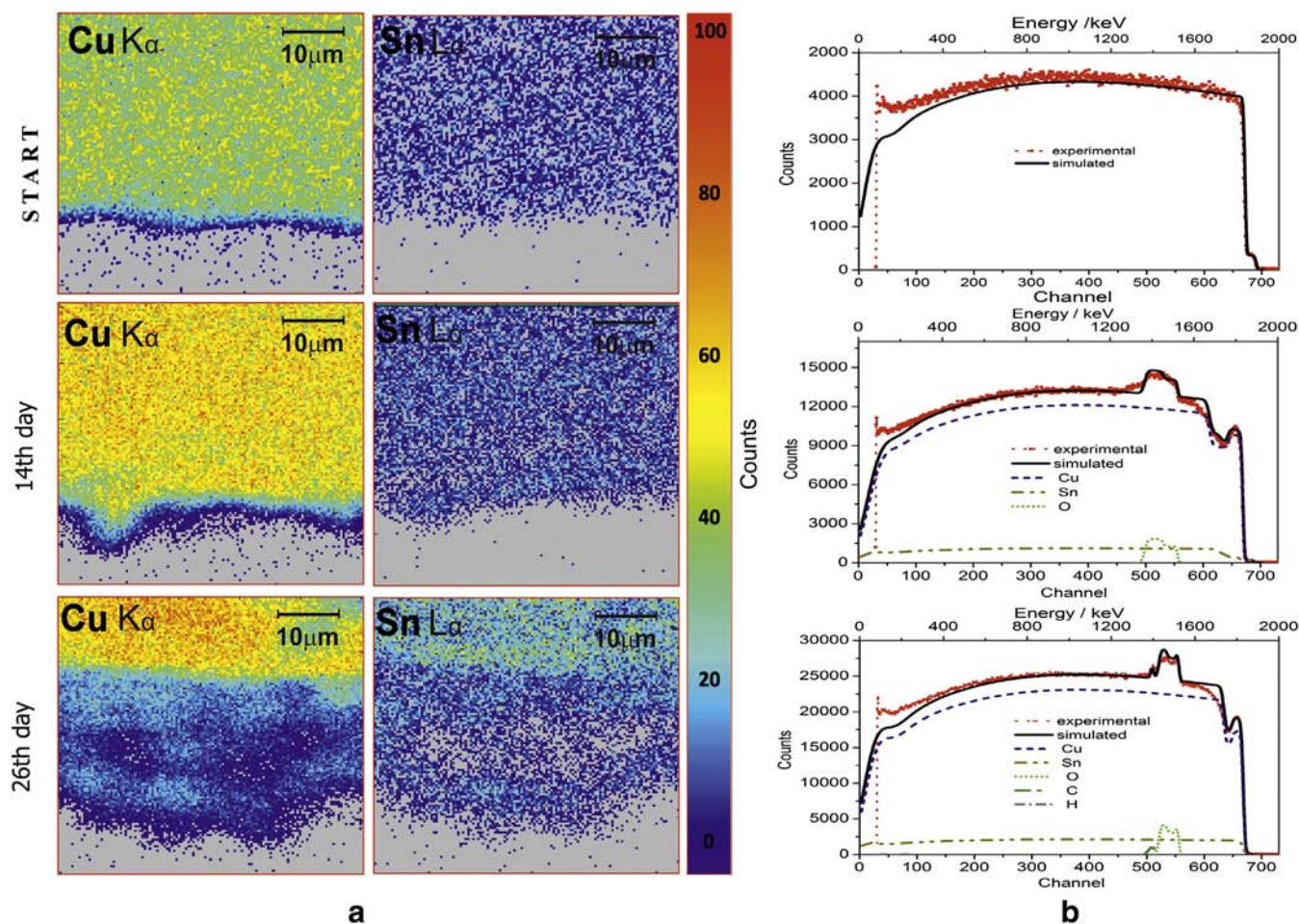
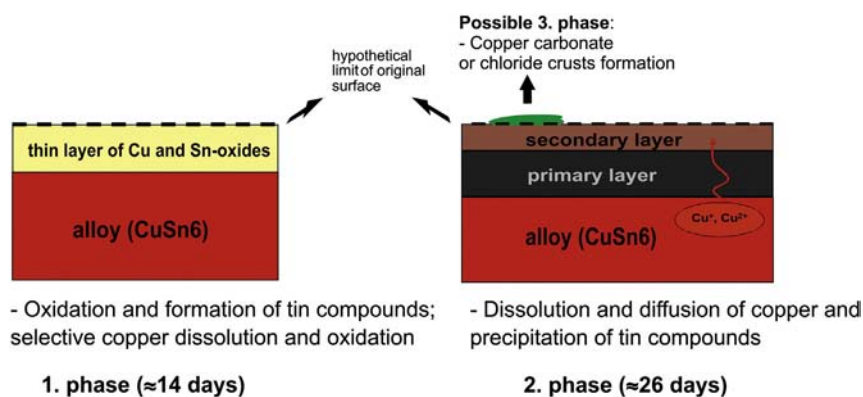


Fig. 3. a) 2D PIXE images (elemental yield distribution for Cu and Sn, scanning area:  $50 \times 50 \mu\text{m}$ ) of the cross sections of the bronze samples after 0, 14 and 26 days of exposure to the simulated low aggressive chloride environment; b) Fitted RBS spectra of the bronze samples after 0, 14 and 26 days of exposure to the chloride corrosion environment. (For interpretation of the references to color in this figure, the reader is referred to the web version of this article.)



**Fig. 4.** Schematic representation of the corrosion layers formed in 0.012 M NaCl during a) 14 days of immersion; b) 26 days of immersion. Compact, thin layer of tin oxide (cassiterite) mixed with copper oxides (cuprite, tenorite) is formed in initial phase. The presence of tin oxide in the layer has a stabilizing effect which results in reduced further dissolution of bulk alloy. In the second phase, another layer composed of cuprous oxides is formed. Process is under diffusion control of copper cations thru the formed compact “tin-rich” layer and the corrosion rate decreases with time leading to a steady state (corrosion rate close to zero) when the outer layer reaches its maximum thickness. These kinds of bilayer structure usually develop under low aggressive corrosion conditions i.e. indoor environment.

and tenorite (CuO). The last, surface layer is composed of copper and oxygen but also contains carbon and was modeled as  $\text{CuCO}_1.3$ .

As discussed in an earlier paper [26], corrosion layer formation on bronze in low aggressive conditions can be described in two phases. Initially, a very thin Sn (II) and Cu (II) oxide film forms at the surface. This primary formed layer possesses high passivating properties. Afterward, copper cations migrate thru the primary layer and precipitate as copper oxides at the surface. At the same time primary, “tin enriched” layer precipitates “in situ” and “moves” towards bulk metal. In that way corrosion progresses in the metal and hypothetical limit of the original surface remains at the same position. After some period of time, corrosion deposit practically reaches its maximum and the corrosion rate decreases to values close to zero (Fig. 4). Possible third, but very slow phase of corrosion progression in moderately aggressive conditions described in literature [17] is incorporation of environmental elements and deposition of their copper compounds (for example copper carbonates or chlorides formation). Presence of porous external deposits covering the outer layer is usually easy to distinguish by color and texture (usually green or bluish–green loose crusts on the surface). These crusts, which were indicated by RBS, cannot be considered as a third layer since they are quite inhomogeneous and do not cover whole corroded surface but are only indicated sporadically on some locations. RBS results yield approximate relative thickness ratios between primary and secondary layer, with the secondary layer being two times thinner than the primary one. Based on above results, schematic representation of corrosion layers formation was given (Fig. 4).

### 3.3. Portable XRF analysis

The quantified results for XRF measurements on non-corroded sample and on samples corroded for 14 and 26 days are reported in Table 1. Calculations were carried out by the XRF-FP software from Amptek, USA, based on the fundamental parameter (FP) approach.

The FP algorithms are commonly used for matrix correction in quantitative analysis of samples of less than infinite thickness. They are

generally based on the knowledge of spectral distribution of the incident radiation and atomic parameters such as fluorescent yields, mass absorption coefficients, transition probabilities etc. [27]. To get higher accuracy, a certified CuSn6 alloy was used as a calibration standard. Accurate composition of the standard alloy is also given in Table 1.

As it can be seen, the results are all in very good agreement with the certified values of the reference material. This proves that the effects of corrosion at this level are still not strong enough to alter the recorded values and to change the accuracy of the XRF measurements, assuming the most intensive lines were used for quantification ( $K\alpha$  for Cu, Sn, P, Fe, Zn, and  $L\alpha$  for Pb). The exception is P, for which the mass fraction is lower for corroded bronze samples than for certified reference bronze, probably due to higher attenuation of low energy P- $K\alpha$  photons (2.013 keV) through the corrosion layer.

Fig. 5 shows two overlaid XRF spectra, recorded on a blank sample and on a sample which was corroded for 26 days. As it can be seen, very little difference can be observed between the two spectra which should show the strongest variance.

However, closer comparison of intensities between the XRF results obtained from 0, 14 and 26 day corroded bronze coupons reveals slight differences between  $K\alpha$  and  $L\alpha$  lines of tin. When the primary radiation from X-ray tube penetrates corroded bronze surface, it is attenuated along its path. A part of the energy of the absorbed photons is converted into fluorescent photons of the elements present in the sample, and some of them reach the surface of the bronze. Recent bronzes are mostly composed of few major elements (mostly copper and tin) which are at the same time the matrix and the elements to be determined. During interpretation of the analytical data obtained for the inhomogeneous samples such as corroded bronzes, knowledge of the depth/volume from which most of the analyte signal originates is essential. The measured intensity of the characteristic X-rays of the tin originates from a well-defined layer of the sample called the critical penetration depth  $t_{\text{crit}}$  which can be calculated from:  $t_{\text{crit}} = 4.61/(\rho\mu_{\text{tot}})$ , where  $\rho$  is the density of the CuSn6 bronze ( $8.8643 \text{ g cm}^{-3}$ ), and  $\mu_{\text{tot}}$  is the sum of the mass attenuation coefficients of the incident and fluorescent

**Table 1**

Chemical composition (wt.%) of the reference bronze used in experiments and XRF-FP software calculated composition from XRF spectra for corroded bronze coupons. Estimated uncertainties calculated by XRF-FP software from Amptek.

Chem. comp. (wt.%)	Cu	Sn	P	Fe	Zn	Pb
CuSn6 reference	93.66	6.10	0.11	0.02	0.10	0.01
CuSn6-0 days	93.58 ± 0.17	6.13 ± 0.20	0.15 ± 0.05	0.02 ± 0.001	0.09 ± 0.001	0.02 ± 0.01
CuSn6-14 days	93.92 ± 0.18	5.94 ± 0.20	0.00 ± 0.00	0.03 ± 0.001	0.07 ± 0.002	0.05 ± 0.01
CuSn6-26 days	93.83 ± 0.18	5.98 ± 0.19	0.03 ± 0.02	0.02 ± 0.001	0.08 ± 0.002	0.05 ± 0.01

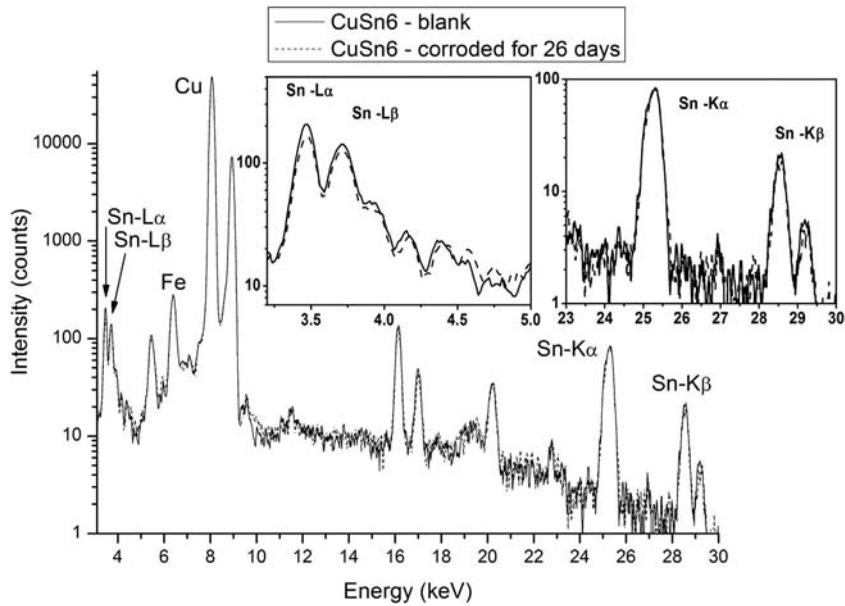


Fig. 5. Overlaid XRF spectra recorded on a blank bronze sample (0 days of exposure; solid line) and on a bronze sample which was exposed to the corrosive environment for 26 days (dashed line). Insertions show low Z and high Z zooms of the same spectra.

radiations multiplied by the cosec of the incident and take-off angles [28]. The critical penetration depth represents the sample thickness from which 99% of the characteristic X-rays originate.

Values of the mass attenuation coefficient for the CuSn6 matrix,  $\mu/\rho$ , were obtained according to simple additivity:

$$\mu/\rho = \sum_i w_i (\mu/\rho)_i \quad (1)$$

where  $w_i$  is the fraction by weight of the  $i^{\text{th}}$  atomic constituent, and the  $(\mu/\rho)_i$  values are taken from the NIST tables [29].  $\mu_{\text{tot}}$  was calculated as a sum of attenuation of incident beam (photon energy just above the critical energy) and attenuation of fluorescent Sn-K $\alpha$ , i.e. Sn-L $\alpha$  radiation (Table 2). If the values for the mass absorption coefficients are substituted in aforementioned Eq. (1), the depth of the irradiated sample with X-rays of the appropriate energy giving rise to 99% of the fluorescent radiation is approx. 118  $\mu\text{m}$  for Sn-K $\alpha$  and 4–5  $\mu\text{m}$  for Sn-L $\alpha$  radiation in CuSn6 bronze matrix, respectively. If we assume that 90% of the characteristic X-rays originate from the surface layer of  $0.5t_{\text{crit}}$  [28] it is obvious that major contribution of Sn-K $\alpha$  radiation comes from the depth of approx. 60  $\mu\text{m}$ , and 2–3  $\mu\text{m}$  for Sn-L $\alpha$ .

When investigating the influence of corrosion layers, further factors have to be taken into account. L $\alpha$  X-ray emission of tin atoms is matrix-sensitive due to its low energy, thus, L $\alpha$  photons emitted from tin atoms will be absorbed more effectively in the presence of heavier matrix i.e. in the bulk alloy (CuSn6) than in the presence of lighter elements, i.e. oxygen forming cuprous oxides in the corrosion layer. If we approximate the corrosion layer and simplify its composition as CuO, the calculated  $t_{\text{crit}}$  for Sn-L $\alpha$  line gives 7.48  $\mu\text{m}$ . Again, taking into account the above mentioned 90% criterion, it can be concluded that majority of Sn-L $\alpha$  signal originates from the first 3–4  $\mu\text{m}$ . If we take into account the

estimated thickness of the corrosion layer for 26th day corroded bronze of 25  $\mu\text{m}$ , we can see that fluorescent Sn-L $\alpha$  radiation originates from the thin top part of the corrosion layer only. Unfortunately, such strong attenuation of Sn-L $\alpha$  line and small value of  $t_{\text{crit}}$  make it impossible to calculate the thickness of the corrosion layer from the Sn-K $\alpha$ /Sn-L $\alpha$  ratio.

Nevertheless, corrosion layer thickness can be estimated from the intensity ratio between Sn-K $\alpha$  lines of the non-corroded (start) and corroded (14th and 26th day) bronze samples. A beam of photons with an incident intensity  $I_0$ , penetrating a layer of material with mass thickness  $x$  and density  $\rho$ , emerges with intensity  $I$  given by the exponential attenuation law:

$$I/I_0 = \exp[-(\mu/\rho)x]. \quad (2)$$

Considering now that the corrosion layer is thin, a fluorescent signal from the bulk elements will be generally visible in the X-ray spectrum, but attenuated by the superimposed layer. Assuming that corrosion layer is composed only of CuO, which is an acceptable approximation, Sn-K $\alpha$  fluorescent radiation would originate only from the bulk CuSn6 bronze. If we replace  $I_0$  from the Eq. (2) by a measured Sn-K $\alpha$  intensity of non-corroded sample, and  $I$  by measured intensity of 14th and 26th day samples, we can calculate mass thickness  $x$ . Obtained value  $x$  now represents the thickness of the corrosion layer of 14 and 26 day corroded bronze, respectively. Calculated corrosion layer thickness from attenuation of Sn-K $\alpha$  line in CuO corrosion layer matrix equals to  $11.17 \pm 0.22 \mu\text{m}$  for 14 day corroded bronze and  $13.11 \pm 0.26 \mu\text{m}$  for 26 day corroded bronze. As can be seen, calculated corrosion layer thicknesses from the attenuation of Sn-K $\alpha$  line through the layer are in good agreement with PIXE results. Thickness value of approx. 25  $\mu\text{m}$  for 26 day corroded bronze was estimated from PIXE elemental map. As it was discussed before (3.2) corrosion layers of

Table 2  
Attenuation coefficients for incident and fluorescent (Sn-K $\alpha$  and Sn-L $\alpha$ ) X-rays in CuSn6 and CuO matrix and information depth and attenuation length for Sn-K $\alpha$  and Sn-L $\alpha$  lines in CuSn6 and CuO matrix. Estimated uncertainties calculated according to Hubbell [30], and Ménesguen and Lépy [31].

Matrix	Attenuation coefficients in $\text{cm}^2\text{g}^{-1}$		$\mu_{\text{tot}}$	Information depth/ $\mu\text{m}$	Attenuation length/ $\mu\text{m}$	$t_{\text{crit.}}/\mu\text{m}$
	Incident X-ray	Fluorescent X-ray				
CuSn6	$14.21 \pm 0.28$ (30 keV)	$21.03 \pm 0.42$ (Sn K $\alpha$ )	$43.94 \pm 0.88$	$182.85 \pm 3.66$	$123.51 \pm 2.47$	$118.36 \pm 2.37$
	$411.53 \pm 20.58$ (4 keV)	$561.14 \pm 28.06$ (Sn L $\alpha$ )	$1204.98 \pm 60.26$	$6.31 \pm 0.32$	$4.63 \pm 0.23$	$4.32 \pm 0.22$
CuO	$8.64 \pm 0.17$ (30 keV)	$17.31 \pm 0.35$ (Sn K $\alpha$ )	$33.12 \pm 0.66$	$421.90 \pm 8.44$	$210.63 \pm 4.21$	$220.41 \pm 4.41$
	$292.32 \pm 14.62$ (4 keV)	$483.54 \pm 24.18$ (Sn L $\alpha$ )	$976.05 \pm 48.80$	$12.47 \pm 0.62$	$7.54 \pm 0.38$	$7.48 \pm 0.37$

26 day corroded bronze are also at some points separated from each other. The outer, separated part, corresponds to the third phase of corrosion processes i.e. incorporation of environmental elements and deposition of their copper compounds (copper-carbonates) and was not considered as the part of the passivating corrosion layer (patina) (Fig. 4). It must be taken into account that corrosion layer is quite rough and uneven. PIXE elemental maps cover only  $50 \times 50 \mu\text{m}$  wide area of a cross-section, whereas XRF beam covers ca.  $1.80 \text{ mm}^2$  of bronze surface (diameter of the beam was set to 1.5 mm). Thus, XRF measurement gives results which are more representative for investigation of large areas than micro-PIXE results, considering the inhomogeneity of the material. Good agreement of the calculated and measured results proves that total amount of tin present in corrosion layer is in concentration that can be neglected for the purpose of this calculation and the corrosion layer can be approximated as pure CuO.

A corrosion layer thickness calculated from attenuation of Sn-L $\alpha$  line was not taken into consideration as the critical depth was estimated at only 7–8  $\mu\text{m}$ . However, the peak intensity of Sn-L $\alpha$  line for 26 day corroded sample is very similar to the Sn-L $\alpha$  intensity for non-corroded bronze (Fig. 5), which indicates the presence of tin in the corrosion layer in the similar amount as in the bulk. Probable explanation lies in the tin distribution in the corrosion layer. The highest amount of tin is present in the layer closest to the bulk and decreases in concentration towards the surface through the corrosion layer. At the same time, matrix density decreases from the bulk towards the surface (from copper oxides and tin oxide close to the bulk to copper carbonates on the surface) i.e. matrix becomes lighter closer to the surface. As the low energy Sn-L $\alpha$  radiation is very matrix sensitive, the higher emission of the L $\alpha$  photons should not be attributed to the higher Sn concentration, but to the increasingly lighter matrix of the corrosion layers.

#### 4. Conclusion

Artificially corroded bronze samples were analyzed by a portable XRF instrument in order to validate this method for obtaining precise bulk metal composition of low corroded artistic bronze artifacts. The method is applied to artificially corroded bronzes with well defined “two-layered” patina formed in sodium-chloride consisting mostly of copper and tin oxides. For precise characterization of the formed corrosion layers two ion beam techniques (PIXE and RBS) were used.

Correlation was established between the portable XRF results and the results obtained with the ion beam techniques. It has been shown that for corrosion layers of up to ca. 25  $\mu\text{m}$  a portable XRF can yield very accurate quantification results. This proves that the effects of corrosion at this level are still not strong enough to alter the measured values for the major elements and to change the accuracy of the XRF measurements. However, when investigating highly corroded bronzes i.e. archaeological artifacts, some damage to the patina of the artifact during sample preparation (polishing) is imminent for a very precise quantification.

Careful examination of the XRF spectra can yield additional information. K $\alpha$  and L $\alpha$  lines of tin fluorescent radiation can give part of the stratigraphic information of the corrosion layer. Small penetration depth of Sn-L $\alpha$  radiation constrains the calculation of the corrosion layer thickness from the Sn-K $\alpha$ /Sn-L $\alpha$  ratio. However, calculated thickness from Sn-K $\alpha$  intensities of non-corroded and corroded samples gives very accurate results. For the corrosion layer a simple CuO composition can be used as a matrix approximation when calculating attenuation of primary and fluorescent radiation through the layer.

#### References

- [1] T. Drayman-Weisser, Dialogue/89. The Conservation of Bronze Sculpture in the Outdoor Environment: A Dialogue Among Conservators, Curators, Environmental Scientists, and Corrosion Engineers, Nace Houston, 1992.
- [2] T.E. Graedel, K. Nassau, J.P. Franey, Copper patinas formed in the atmosphere – I. Introduction, *Corros. Sci.* 27 (1987) 639–659.
- [3] E. Johansson, C. Leygraf, B. Rendahl, Comparison of Different Methods for Assessment of Corrosivity in Indoor Environments, 13th International Corrosion Congress, Melbourne, Australia, 1996.
- [4] A.R. Mendoza, F. Corvo, Outdoor and indoor atmospheric corrosion of non-ferrous metals, *Corros. Sci.* 42 (2000) 1123–1147.
- [5] C. Chiavari, K. Rahmouni, H. Takenouti, S. Joiret, P. Vermaut, L. Robbiola, Composition and electrochemical properties of natural patinas of outdoor bronze monuments, *Electrochim. Acta* 52 (2007) 7760–7769.
- [6] C. Chiavari, A. Colledan, A. Frignani, G. Brunoro, Corrosion evaluation of traditional and new bronzes for artistic castings, *Mater. Chem. Phys.* 95 (2006) 252–259.
- [7] N. Kallithrakos-Kontos, A.A. Katsanos, A. Aravatinos, M. Oeconomides, I. Touratsoglou, Study of ancient Greek copper coins from Nikopolis (Epirus) and Thessaloniki (Macedonia), *Archaeometry* 35 (1993) 265–278.
- [8] C.P. Swan, S.J. Fleming, M. Jaksic, Recent applications of PIXE spectrometry in archaeology. I: characterization of bronzes with special consideration of the influence of corrosion processes on data reliability, *Nucl. Instr. Meth. B* 64 (1992) 499–504.
- [9] G. Vittiglio, K. Janssens, B. Vekemans, F. Adams, A. Oost, A compact small-beam XRF instrument for in-situ analysis of objects of historical and/or artistic value, *Spectrochim. Acta Part B* 54 (1999) 1697–1710.
- [10] A. Longoni, C. Fiorini, P. Leutenegger, S. Sciuti, G. Fronterotta, L. Strueder, P. Lechner, A portable XRF spectrometer for non-destructive analyses in archaeology, *Nucl. Instrum. Meth.* (1998) 407–409.
- [11] A. Adriaens, Non-destructive analysis and testing of museum objects: an overview of 5 years of research, *Spectrochim. Acta Part B* 60 (2005) 1503–1516.
- [12] In: K. Tsuji, J. Injuk, R. Van Grieken (Eds.), *X-ray Spectrometry: Recent Technological Advances*, Wiley, New York, 2004.
- [13] A. Denker, W. Bohne, J. Opitz-Coutureau, J. Rauschenberg, J. Rohrich, E. Strub, Influence of corrosion layers on quantitative analysis, *Nucl. Instr. Meth. B* 239 (1992) 65–70.
- [14] D. Mudronja, M. Jakšić, S. Fazinić, I. Božičević, V. Desnica, J. Woodhead, Z. Stos-Gale, Croatian Appoxiomenos alloy composition and lead provenance study, *J. Archaeol. Sci.* 37 (2010) 1396–1402.
- [15] A. Markowicz, Portable X-ray Fluorescence Spectrometry – Capabilities for In Situ Analysis, in: P.J. Potts, M. West (Eds.), RSC Publishing, Cambridge, 2008, p. 13.
- [16] G.L. Molnar, Handbook of Prompt Gamma Activation Analysis with Neutron Beams with CDROM, Kluwer Academic Publishers, 2003.
- [17] L. Robbiola, J.M. Blengino, C. Fiaud, Morphology and mechanisms of formation of natural patinas on archaeological Cu–Sn alloys, *Corros. Sci.* 40 (1998) 2083–2111.
- [18] D. Hallam, D. Thurrowgood, V. Otieno-Alego, D. Creagh, A. Viduka, Studies of Commercial Protective Petrochemical Coatings on Ferrous Surfaces of Historical and Museum Objects, Metal in: I. MacLeod, J.M. Theile, C. Degrygn (Eds.), Proceedings of the International Conference on Metals Conservation, Santiago (Chile), Western Australian Museum, Welshpool, 2001, pp. 297–303.
- [19] ASTM G 31-72, Standard practice for laboratory immersion corrosion testing of metals (1990) 102–109.
- [20] M. Bogovac, I. Bogdanović, S. Fazinić, M. Jakšić, L. Kukec, W. Wilhelm, Data acquisition and scan control system for nuclear microprobe and other multiparameter experiments, *Nucl. Instr. Meth. B* 89 (1994) 219–222.
- [21] E. Rauhala, N.P. Barradas, S. Fazinić, M. Mayer, E. Szilágyi, M. Thompson, Status of ion beam data analysis and simulation software, *Nucl. Instr. Meth. B* 244 (2006) 436–456.
- [22] SIGMACALC calculator (<http://www.nds.iaea.org/sigmacalc/>).
- [23] M. Blaauw, J.L. Campbel, S. Fazinić, M. Jakšić, I. Orlić, P. Van Espen, The 2000 intercomparison of PIXE spectrum analysis software, *Nucl. Instr. Meth. B* 189 (2002) 113–122.
- [24] M. Jakšić, I. Bogdanović Radović, M. Bogovac, V. Desnica, S. Fazinić, M. Karlušić, Z. Medunić, H. Muto, Ž. Pastuović, Z. Siketić, N. Skukan, T. Tadić, New capabilities of the Zagreb ion microbeam system, *Nucl. Instr. Meth. B* 260 (2007) 114–119.
- [25] P. Piccardo, B. Mille, L. Robbiola, Tin and Copper Oxides in Archaeological Bronzes, in: P. Dillman, G. Beranger, P. Piccardo, H. Matthiesen (Eds.), *Corrosion of Metallic Heritage Artefacts*, Woodhead Publishing Limited, Cambridge, England, 2007, pp. 239–260.
- [26] D. Šatović, L. Valek Žulj, V. Desnica, S. Fazinić, S. Martinez, Corrosion evaluation and surface characterization of the corrosion product layer formed on Cu–6Sn bronze in aqueous Na<sub>2</sub>SO<sub>4</sub> solution, *Corros. Sci.* 51 (2009) 1596–1603.
- [27] R. Sitko, Quantitative X-ray fluorescence analysis of samples of less than “infinite thickness”: difficulties and possibilities, *Spectrochim. Acta Part B* (2009) 1161–1172.
- [28] A. Markowitz, An overview of quantification methods in energy-dispersive X-ray fluorescence analysis, *Pramana J. Phys.* 76 (2011) 321–329.
- [29] J.H. Hubbell, S.M. Seltzer, Tables of X-Ray Mass Attenuation Coefficients and Mass Energy-Absorption Coefficients from 1 keV to 20 MeV for Elements Z = 1 to 92 and 48 Additional Substances of Dosimetric Interest, Radiation and Biomolecular Physics Division, 1990.
- [30] J.H. Hubbell, Compilation of photon cross-sections: some historical remarks and current status, *X-Ray Spectrom.* 28 (1999) 215–223.
- [31] Y. Ménesguen, M.-C. Lépy, Mass attenuation coefficients in the range  $3.8 \leq E \leq 11 \text{ keV}$ , K fluorescence yield and K $\beta$ /K $\alpha$  relative X-ray emission rate for Ti, V, Fe, Co, Ni, Cu and Zn measured with a tunable monochromatic X-ray source, *Nucl. Instr. Meth. B* 268 (2010) 2477–2486.